BNL-207817-2018-JAAM

A Linear Array of Position-Sensitive Virtual Frisch-Grid CdZnTe for Low-energy Gamma Rays

L. Ocampo Giraldo,

To be published in "Nuclear Inst. and Methods in Physics Research, A"

July 2018

Nonproliferation and National Security Department

Brookhaven National Laboratory

U.S. Department of Energy

USDOE National Nuclear Security Administration (NNSA), Office of Nonproliferation and Verification Research and Development (NA-22)

Notice: This manuscript has been authored by employees of Brookhaven Science Associates, LLC under Contract No. DE-SC0012704 with the U.S. Department of Energy. The publisher by accepting the manuscript for publication acknowledges that the United States Government retains a non-exclusive, paid-up, irrevocable, world-wide license to publish or reproduce the published form of this manuscript, or allow others to do so, for United States Government purposes.

DISCLAIMER

This report was prepared as an account of work sponsored by an agency of the United States Government. Neither the United States Government nor any agency thereof, nor any of their employees, nor any of their contractors, subcontractors, or their employees, makes any warranty, express or implied, or assumes any legal liability or responsibility for the accuracy, completeness, or any third party's use or the results of such use of any information, apparatus, product, or process disclosed, or represents that its use would not infringe privately owned rights. Reference herein to any specific commercial product, process, or service by trade name, trademark, manufacturer, or otherwise, does not necessarily constitute or imply its endorsement, recommendation, or favoring by the United States Government or any agency thereof or its contractors or subcontractors. The views and opinions of authors expressed herein do not necessarily state or reflect those of the United States Government or any agency thereof.

A Linear Array of Position-Sensitive Virtual Frisch-Grid CdZnTe for Low-energy Gamma Rays

L. Ocampo Giraldo, A. E. Bolotnikov, G. S. Camarda, G. De Geronimo, J. Fried, D. Hodges, A. Hossain, E. Vernon, and R. B. James

***Abstract*— Large-area arrays of position-sensitive virtual Frisch-grid CdZnTe (CZT) detectors with enhanced energy resolution and high efficiency have been proposed for spectroscopy and imaging of gamma-ray sources. Here, we present the design and test results of a linear array of such detectors optimized for use in handheld instruments. There are several application areas for such detectors including uranium enrichment measurements, storage monitoring, dosimetry and other nuclear safeguards related tasks. The array configuration provides a large area with minimum number of readout channels, which potentially allows the developers to avoid using ASIC-based readout electronics by substituting it with hybrid preamplifiers followed by digitizers. The array prototype consists of 6 5x7x25 mm^3 CZT detectors side-oriented with respect to the source to achieve the maximum area. Each detector is furnished with 5 mm-wide charge-sensing pads placed near the anode. As an option, the pads can be grouped together to reduce the number of readout channels. The same can be done with the cathodes. The pads signals are converted into X–Y coordinates and combined with the cathode signals (for the Z coordinates) to give 3D positional information of each interaction point. This information is used to correct the response non-uniformity caused by material inhomogeneity, which allows the developers to use standard grade (unselected) CZT crystals, while retaining high spectroscopic performance.**

***Index Terms*—CdZnTe, high-granularity detectors, 3D position-sensitive virtual Frisch-grid detectors, crystal defects, charge-loss correction**

I. Introduction

Arrays of position-sensitive virtual Frisch-grid (VFG) CdZnTe (CZT) detectors offer high detection efficiency, high energy resolution and a capability to correct response non-uniformity [1,2] which allows the developers to use standard-grade (unselected) material, while retaining high performance. Previously we demonstrated the feasibility of using position-sensitive VFG detectors with thicknesses up to 5 cm and array prototypes consisting of small numbers of detectors coupled with a front-end ASIC resulting in an energy resolution of <1% FWHM at 662 keV after corrections. The second prototype was a 4x4 array with an energy resolution of ~0.9% FWHM at 662 keV after corrections with a position resolution <500μm [3]. The arrays provide performance and functionality comparable to 3D pixelated detectors but at a lesser cost. The potential applications of the arrays, which can be configured into detection planes with different geometrical form factors and dimensions, includes nuclear security, non-proliferation, safeguards, medical imaging, X- and gamma-ray astronomy, and other areas which require spectroscopy and imaging of gamma-ray sources in a wide dynamic range, from ~10 keV up to several MeV. In this work, we present the results from testing a small linear array of six position-sensitive VFG detectors optimized for usage in compact handheld instruments for uranium enrichment measurements, storage monitoring, dosimetry and other safeguards-related tasks.

The virtual Frisch-grid design was originally proposed for a noble gas ionization chamber with a long drift region [4]. This design approach was also adopted for CZT (and some other semiconductor detectors) and was used in CAPture^{TM} [5], hemispherical [6], Frisch-ring [7], and capacitive Frisch-grid [8] detectors. In our detectors, the virtual Frisch-grid shielding effect is achieved by using 4 charge-sensing pads attached to the side surfaces near the anode. These non-contacting, virtually grounded electrodes play similar roles as those used in Frisch-grid [7] and capacitive Frisch-ring [8] detectors. The difference is that we also use the pads for position sensing. The signal readouts from the pads are converted into X-Y coordinates, while the drift time and the cathode-to-anode ratio, C/A, is used to determine the Z coordinate associated with the location of each interaction event.

II. Array design

The array consisted of six VFG detectors fabricated from 5x7x25 mm^3 CZT crystals acquired from Redlen, Inc. The number of crystals was dictated by size of the detector board, which we adopted from our previous project [3]. The detectors have a simple design. Each crystal, furnished with two gold contacts on the top and bottom surfaces (the anode and the cathode) is

This work was supported by the U.S. Department of Energy, Office of International Nuclear Safeguards, Safeguards Technology Development Subprogram. This manuscript has been authored by Brookhaven Science Associates, LLC under Contract No. DE-AC02-98CH1-886 with the U.S. Department of Energy.
L. Ocampo Giraldo (phone: 631-344-8364; e-mail: locampo@bnl.gov), A. E. Bolotnikov, G.S. Camarda, G. De Geronimo, J. Fried, A. Hossain, E. Vernon are with Brookhaven National Laboratory, Upton, NY 11793, USA.
D. Hodges is with University of Texas at El Paso, El Paso, TX 79968, USA.
R. B. James is with Savannah River National Laboratory, Aiken, SC 29803, USA.

encapsulated inside the ultra-thin polyester shell for electrical insulation and mechanical protection of the detector, as we previously described [2]. The shell tightly envelops the crystal and holds in place two CuBe flat-spring contacts on the cathode and the anode faces. Four 5-mm wide pads, cut from copper adhesive foil, are attached over the shell near the anode side.

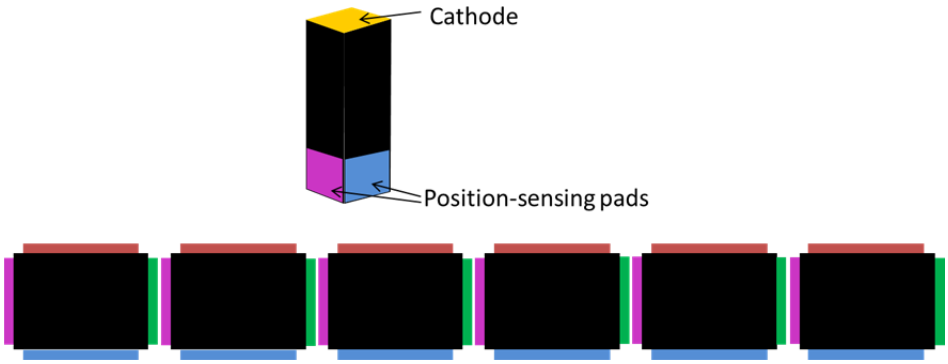

Figure 1. Schematic of all six VFG detectors identifying the position of their respective pads.

The detectors were placed vertically on the detector board and gently pressed from the top using the cathode board having the decoupling capacitors and resistors. The anode spring contacts touch the designated anode pads on the board, while the charge-sensing pads are soldered to the board contacts. The signals generated by the incident photons on the anodes, cathodes and 4 position-sensing pads are routed to the corresponding front ASIC inputs (charge-sensitive preamplifiers). The decoupling circuitries are required for reading the signals from cathodes, which are biased at 2500-3000 V. Fig. 2 shows the image of the fully assembled array consisting of 6 detectors squeezed between the cathode and the detector boards.

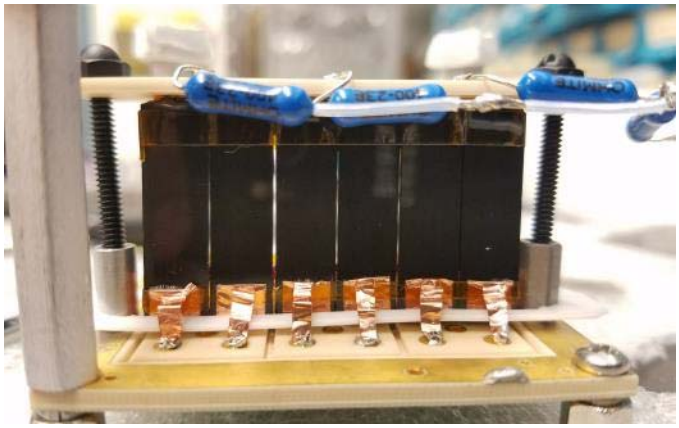

Figure 2. Frontal view of the linear array with one side of pads connected to the PCB board.

The detector board, with the detectors on the front and the multipin connectors on the opposite side, was plugged into the motherboard inside the test box (see Fig. 3). The motherboard also carries the ultra-stable low-voltage passive converters supplying power to the ASIC chips, two analog-to-digital converters (ADCs) for digitizing the peak amplitudes from all channels, the Field Programmable Gate Array (FPGA) for processing the data and communicating with the ASICs and the USB port [10-12].

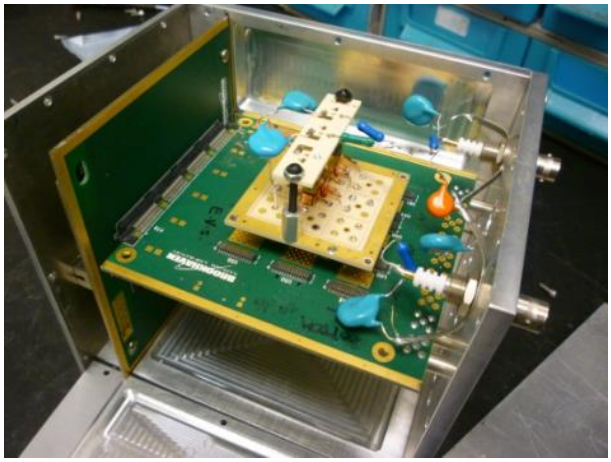

Figure 3. Linear Array mounted to the circuit board inside the aluminum test box.

The AVG1 ASIC used in these measurements [2] allowed us to capture the signals from individual cathodes, anodes and pads which would require 36 readout channels in the case of 6 detector arrays. The ASIC was developed for conventional VFG detectors and employs the same design implemented for H3D pixelated detectors [10-12]. The AVG ASIC has 6 inputs for the negative polarity signals induced on the cathodes and 36 channels with slightly shifted baseline so both polarity signals, which are generated in the pixelated detector, can be captured. These 36 inputs could be used for reading the positive signals generated on the anodes and the negative signals on the pads. The only limitation of the current AVG ASIC is that it has a limited dynamic range for the negative signals. Thus, if the deposited energies are >1 MeV some fraction of the pad signals will be clipped and the position will not be evaluated correctly. We found that the effect of the pad signal clipping become notable for the gamma rays above 1 MeV. We are currently developing a new ASIC that will have a wider dynamic range for the negative signals.
To calculate the normalized X and Y coordinates, we used the center of gravity method:

$$X = \frac{A_x^1}{A_x^1 + A_x^2} \tag{7}$$

and

$$Y = \frac{A_y^1}{A_y^1 + A_y^2}, \tag{8}$$

where A_x^1, A_x^2, A_y^1 and A_y^2 are signal amplitudes measured from the pairs of opposite pads along the X and Y directions. For the Z coordinate we used the C/A ratio. As we described previously [2], this approximation is sufficient for correcting the response non-uniformity. The measured X-Y-Z values constitute a configuration space, which correlates to the spatial variations in the measured anode signals. Thus, by segmenting the X-Y-Z space into small voxels we can differentiate the signals corresponding to each of the voxels and apply a charge-loss correction accordingly using a 3-dimensional correction matrix (CM) generated during calibration [2]. For comparison purposes, we also apply drift-time corrections, along the Z direction, which are called 1D corrections.

One of our goals was to investigate the possibility of making a detector with a reduced number of readout channels. We tested several options for combining the cathode and the charge-sensing pads (e.g. using one input for reading signals from several pads or cathodes). In the case of low-energy photons with low probability of having multiple interaction points, using the combined pads does not create any ambiguity problems related to multiple interaction locations associated with each incident gamma-ray. We demonstrated that we could combine several pads belonging to different detectors because there is no leakage current on the charge-sensing pads. Therefore we were able to interconnect all pads in 4 groups and use only 4 individual inputs. The schematic in Fig. 1 also shows the pad grouping in four different colors. We also demonstrated that 2 and even 4 cathodes could be connected to a single cathode input. Fig. 2 shows the cathodes and the pads from two adjacent detectors connected together, while the outside pads and the anodes were read out individually. For this particular configuration we used 6 anodes, 3 cathodes and 18 pad channels (a total of 27 channels). In the case of the most “economical” configuration, it will suffice to have 2 cathodes, 6 anodes and 4 pad channels (totaling 12 channels).

Another goal was to evaluate the temperature stability of the array in the field under real conditions. To protect the detector and electronics from the moisture that can easily condense during the temperature cycling, we fabricated a special plastic enclosure, made of VeroBlackPlus RGD875, that hermetically seals the entire system: the detector and electronics (see Fig. 4). The enclosure also allowed us to control the temperature in both the lab and field environments. For this purpose, we use a massive aluminum flange to seal the enclosure and dissipate heat. When the test box is placed inside the enclosure the flange touches a copper block firmly bolted to the backside cover of the test box used for conducting the heat generated by the readout electronics and FPGA. Considering the high-temperature conditions expected for the field measurements, we attached a commercial 40W Peltier cooler to the outer flange to maintain a reasonably stable temperature, +/-1 °C, for the detectors. As we show next, the main temperature instability does not come from the ASIC, but the temperature dependence of the charge

collection efficiency of the detectors. This was found to be significant enough to affect the energy resolution if the temperature was not kept stable within ~1.0-1.5 degrees. Using an environmental enclosure and the cooler, we measured the detector responses at different temperatures between 15 and 40 °C. We found that the detectors could operate at a temperature close to 30 °C without significantly affecting the energy resolution. Above 30 °C the resolution degrades and approaches 2% at 662 keV at 40 °C. We took only a few measurements at temperatures above 35 °C because, as we discovered, some of the detectors kept at high bias for several days at elevated temperatures suddenly became leaky and needed to be replaced. To avoid damaging the detectors, we took fewer measurements at temperatures above 35 °C. We note that we fabricated and used such a bulky environmental enclosure for the entire test box as it was the simplest (low cost) solution in preparation for the field tests. In the actual instrument, only the detectors and front-end electronics require environmental protection. Furthermore, as is seen in Fig. 4, the enclosure has specially designed slots for attaching the shielding tungsten plates and the front tungsten window, if necessary. Here we presented the results obtained in our labs using the standard sealed radioactive sources.

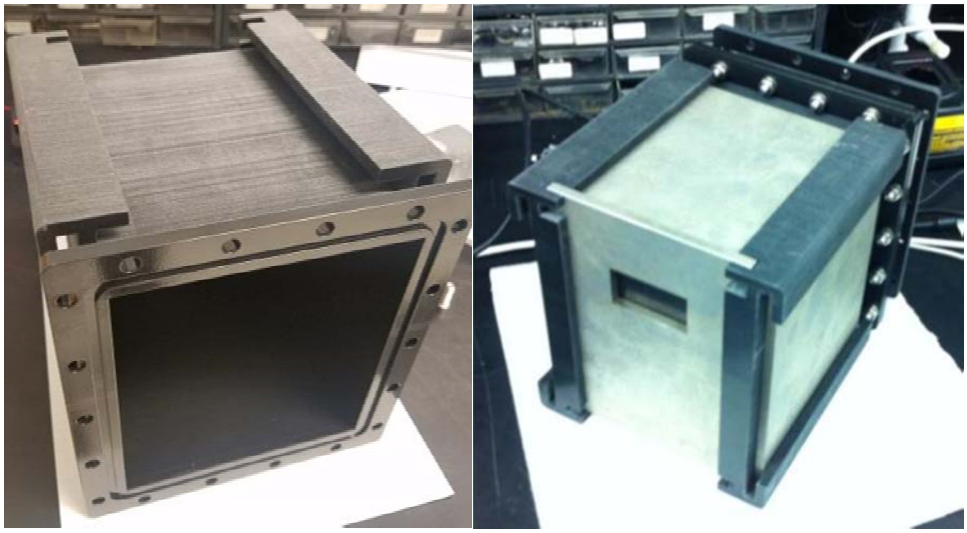

Figure 4. (a) A 3D printed plastic waterproof enclosure. (b) Plastic waterproof enclosure with tungsten plates surrounding it.

III. TEST RESULTS

The calibration for each detector was done at several temperatures and using several gamma-ray lines. For calibration we collected the pulse-height spectra from known gamma-ray sources and used them to evaluate the channels' baselines, gains and the 3D correction matrixes for each detector. For presenting the results, we collected additional data sets (not used for calibration) to avoid any correlation effect, e.g., if we apply the correction matrix to the same data used for its evaluation, we can get an energy resolution as good as 0.3% at 662 keV, which is an erroneous result. Fig. 5 shows 3 rows of the spectra: after applying 3D corrections (top), 1D (middle) correction only, and the raw data (bottom) measured from a fresh fuel rod, ~93% ^{235}U, located ~40 cm from the detector plane. The measurements were taken at a temperature of ~19 °C. The same cathode bias of 2750 V was applied to all detectors. Fig. 6 shows the combined spectra after 3D and 1D corrections, correspondingly. The energy resolution was found to be 1.9 % FWHM at 186 keV, which is very good for such big detectors with an area of 5x7 mm^2. If we only apply a 1D correction, the energy resolution is only ~3%. We note that the electronic noise (due to leakage current) is the major factor limiting the energy resolution of these detectors.

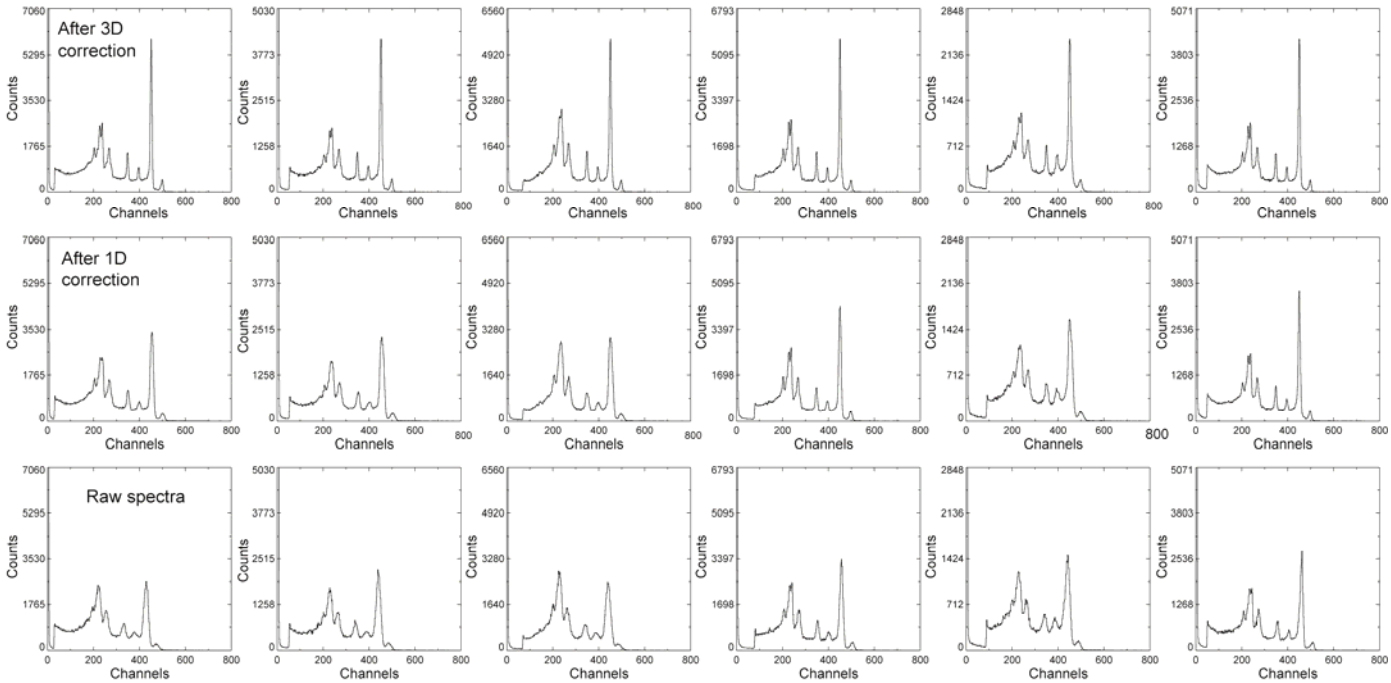

Figure 5. The pulse-height spectra measured at 19°C and corrected using calibration data measured at the same temperature.

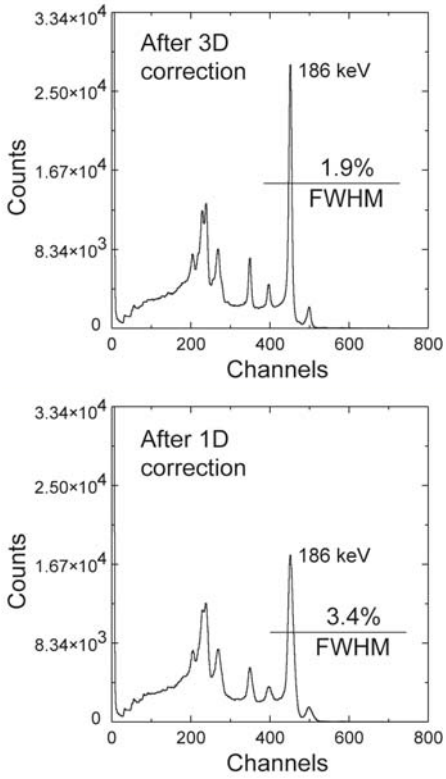

Figure 6. The combined spectra, for ^{235}U, from all 6 detectors after (top) and before (bottom) 3D corrections.

Similar to the previous plot, Fig. 7 shows ^{133}Ba spectra measured at 20°C. The cathode bias is 2500 V. The bottom row shows the raw data clearly displaying a poor resolution for multiple peaks close to each other. The middle row is the spectra after the 1D correction. The top row shows a significant improvement in the resolution, visibly distinguishing the 303 keV peak from the 356-keV and 383-keV peaks.

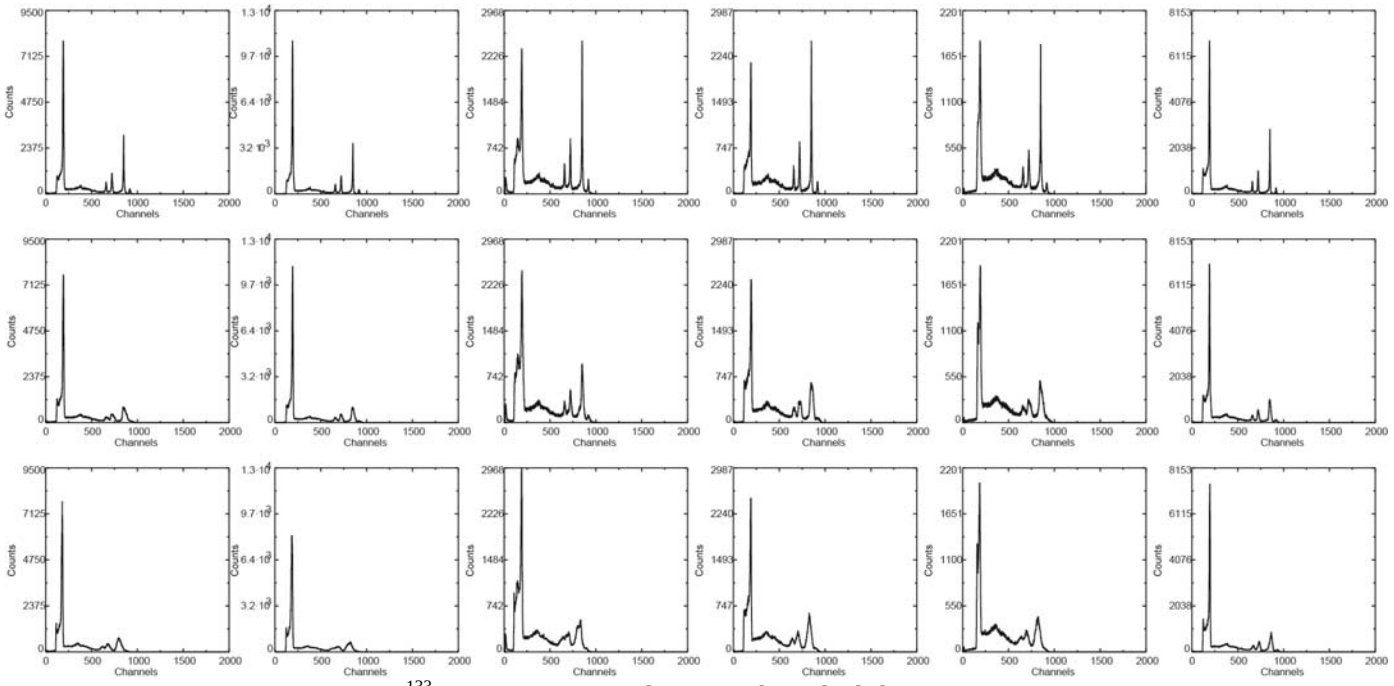

Figure 7. ^{133}Ba spectra measured at 20C. The cathode bias is 2500 V.

The position sensitivity allowed us to evaluate the distributions of the photopeak positions and counts over the area of each detector (response maps). As an example, Fig. 8 shows the 60x60 pixel maps of the photopeak counts measured from the individual voxels. The maps clearly show the prismatic punching defects (scars) inside the CZT crystals which can be found in most standard-grade CZT material [4]. These maps also illustrate that good position resolutions are achievable with the charge sensing pads.

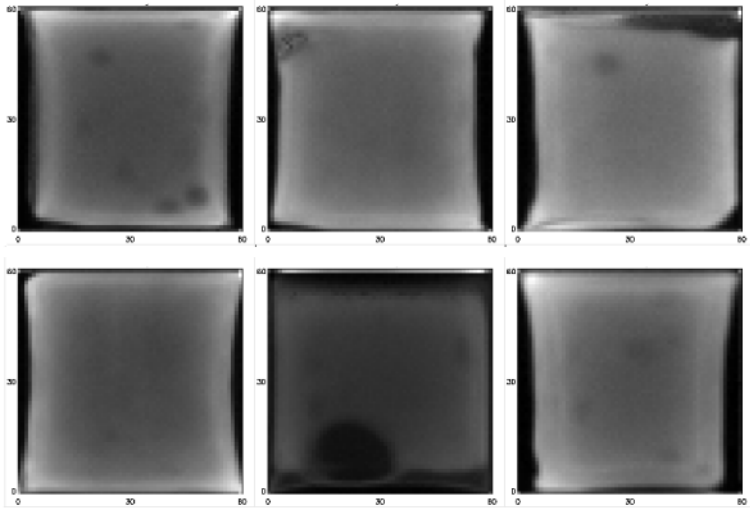

Figure 8. 60x60 pixel maps of the photopeak counts measured from the individual voxels for the six different detectors.

Temperature stability measurements are illustrated in Fig. 9. It shows 5 rows of plots representing changes of the baselines, the photopeak width (FWHM) and gains as the detector temperature gradually decreases from 31 °C down to 18 °C. For these data we used the calibration and correction matrix generated at 31 °C. The temperature time profiles are shown in the last row (same for all detectors). Every point in the plots was evaluated using the ^{137}Cs spectra accumulated for ~3 min with ~20 min intervals. The temperature was monitored using two thermocouples attached with copper tape to the detector board ~1 cm away from the detectors. The first row shows the photopeak position. On average, the photopeak position shifts ~20 keV and remains stable, <1 keV, so long as the temperature remains constant. The second row shows the changes of the anode baselines, which are almost negligible, <1.5 keV, indicating the high temperature-stability of the readout ASIC. This means that the main reason for the photopeak shift is the detectors themselves; the charge-collection efficiency depends on the temperature. Furthermore, it also demonstrates the importance of stabilizing the temperature within +/-1 degree during the measurements. The operation point

can be chosen in a broad range of temperatures, but it should be stable to ensure the best energy resolution. The third row shows the dependence of FWHM of the photopeaks, which are in the range 5-7 keV and remain nearly independent of temperature. Detectors 3 and 4 show slight improvements in their energy resolution. These improvements were unexpected since the response matrix was generated at an elevated temperature, 31 °C, and the detectors may have some extra electronic noise due to their state after exposure to the higher temperatures.

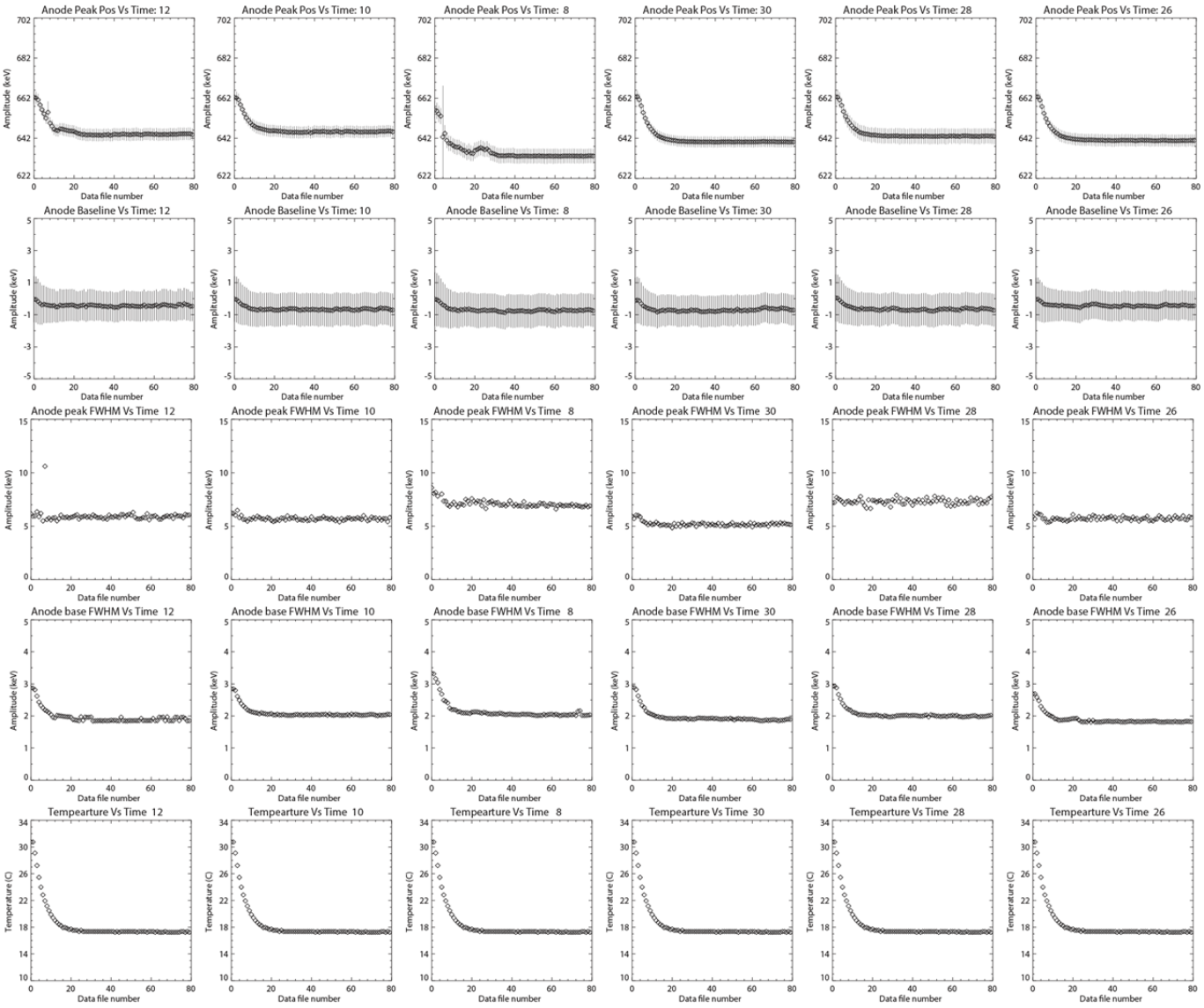

Figure 9. Changes of the baselines and gains of six detectors from the array as the detector temperature gradually decreases from 31 °C down to 18 °C. Every point represents the spectra accumulated for about 3 min with 20 min intervals. The temperature was monitored using a thermocouple placed on the detector board near the detectors. The calibration data set was generated at 31 °C.

Fig. 10 represents the same raw data as in the previous example but processed using the calibration and correction matrix generated at 18 °C (the ending point in the temperature profile). The plots demonstrate similar behaviors for the photopeaks and baselines compared to the previous case; however, the FWHMs of the photopeaks decrease as the temperature goes down and are fully correlated with the temperature profiles. The initial widths are nearly the same as in the previous case but have decreased down to ~5 keV, which reflects energy-resolution improvements at low temperatures due to the decreasing leakage current and corresponding reductions of the electronic noise, as expected. We note that the starting photopeak widths (at 31 °C) are slightly broader than the corresponding width shown in the previous example, but at 19 °C they are virtually the same as in the previous case. This means that the correction matrix is practically independent of temperature (if we neglect a small contribution from the electronic-noise increase at elevated temperatures). This also means that it is important to stabilize the temperature within +/-1 degree °C during the measurements. Otherwise, gain changes will cause broadening of the photopeaks. Alternatively, one can adjust the gains according to temperature variations, while using the same correction matrix. Furthermore, it is better to use the

correction matrix generated at a temperature which is close to or lower than the temperature at which measurements are to be taken.

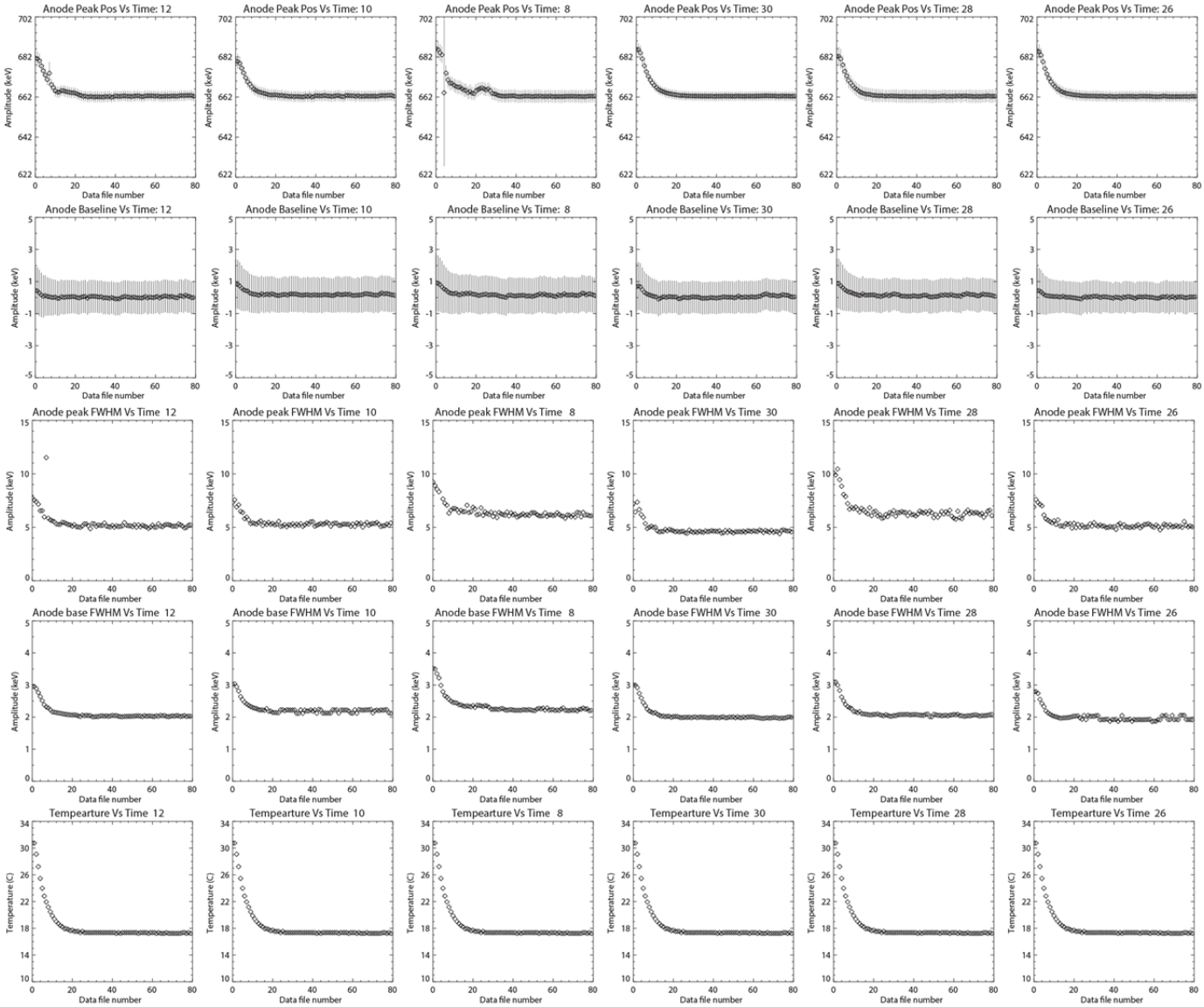

Figure 10. Plots representing the same data as in Fig. 8 but with the calibration files generated at 19 °C.

Spectra in Fig. 11(a-f) illustrate the weak temperature dependence of the correction matrix. The ^{137}Cs spectra (a) and (b) were measured at 31°C and processed using the correction matrix generated for a 662 keV gamma line at 31 and 18 °C, respectively. The spectra (c) and (d) were measured from two sources: ^{232}U and ^{137}Cs at 18 °C and processed using the correction matrix generated for a 662 keV line at 31°C and 18°C. We note, that in these examples, the correction matrix generated at 662 keV works very well for low energies, e.g., 238 keV. Finally, spectra (e) and (f) from ^{232}U were measured at 31 °C and processed using the correction matrix generated for a 662-keV gamma line at 31 and 18 °C, respectively.

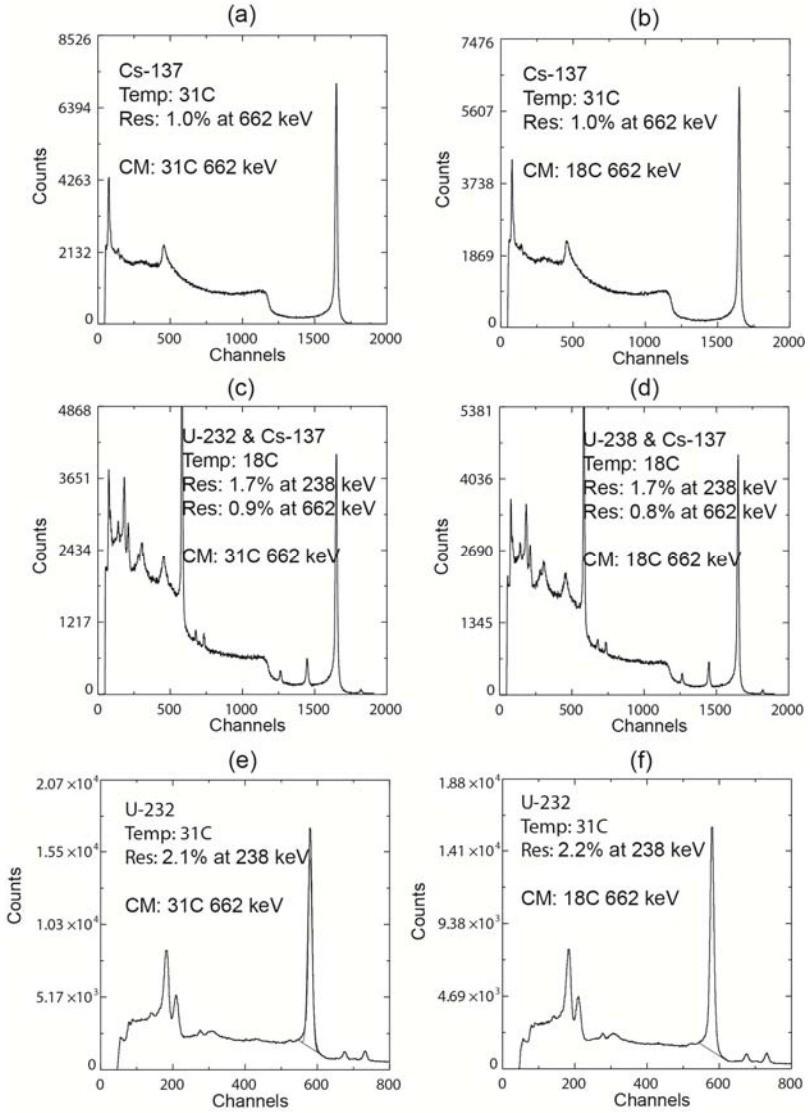

Figure 11(a-f). Combined spectra from six detectors illustrating the temperature independence of the correction matrix (CM). The Cs-137 spectra (a) and (b) were measured at 31 °C and processed using CM generated using a 662-keV line at 31 and 18 °C, while the spectra (c) and (d) were measured from two sources: U-232 and Cs-137 at 18 °C and processed using CM generated using 662-keV line at 31°C and 18 °C, as well. Spectra (e) and (f) are from U-232 measured at 31°C and processed using CM generated using a 662-keV line at 31 and 18 °C, respectively.

As previously mentioned, one of our goals was to make a detector with a minimum number of readout channels. With this in mind we investigated the possibility of interconnecting the pads corresponding to each of the four sides of all the detectors (see the schematic in Fig. 1 showing the pad grouping in four different colors). This resulted in only 4 readout channels being used to read signals from all pads. This can create an ambiguity problem for multiple interaction point events but for low-energy gamma rays it should work as if all pads are readout individually. Therefore only 10 channels are needed to read all the signals: 4 pads and 6 anodes. To test this approach we took measurements of spectra from the ^{232}U source. For these measurements we connected the cathodes together without increasing the electronic noise. We note that the cathode signals are needed to evaluate the Z-coordinates of the interaction points. However, if the waveform processing technique is used to process the data then one can substitute the cathode signals with the sum of the pads signals. In this case no cathode readout channels will be required at all. Thus it is possible to reduce the total number of channels to 10 for the 10 cm^2 area detector. This will also simplify the detector design by eliminating decoupling capacitors and the cathode signals wires. Furthermore, one can avoid using an ASIC by replacing it with hybrid preamplifiers and a 10-channel digitizer. Fig. 12 shows the ^{232}U pulse-height spectra from individual detectors after 3D corrections (top), 1D correction (middle) and raw data (bottom) measured for the detector configurations with all pads interconnected. The temperature was 20°C and the cathode bias was 2500 V. The energy resolution was in the range (2.0-2.2)% after the 3D corrections.

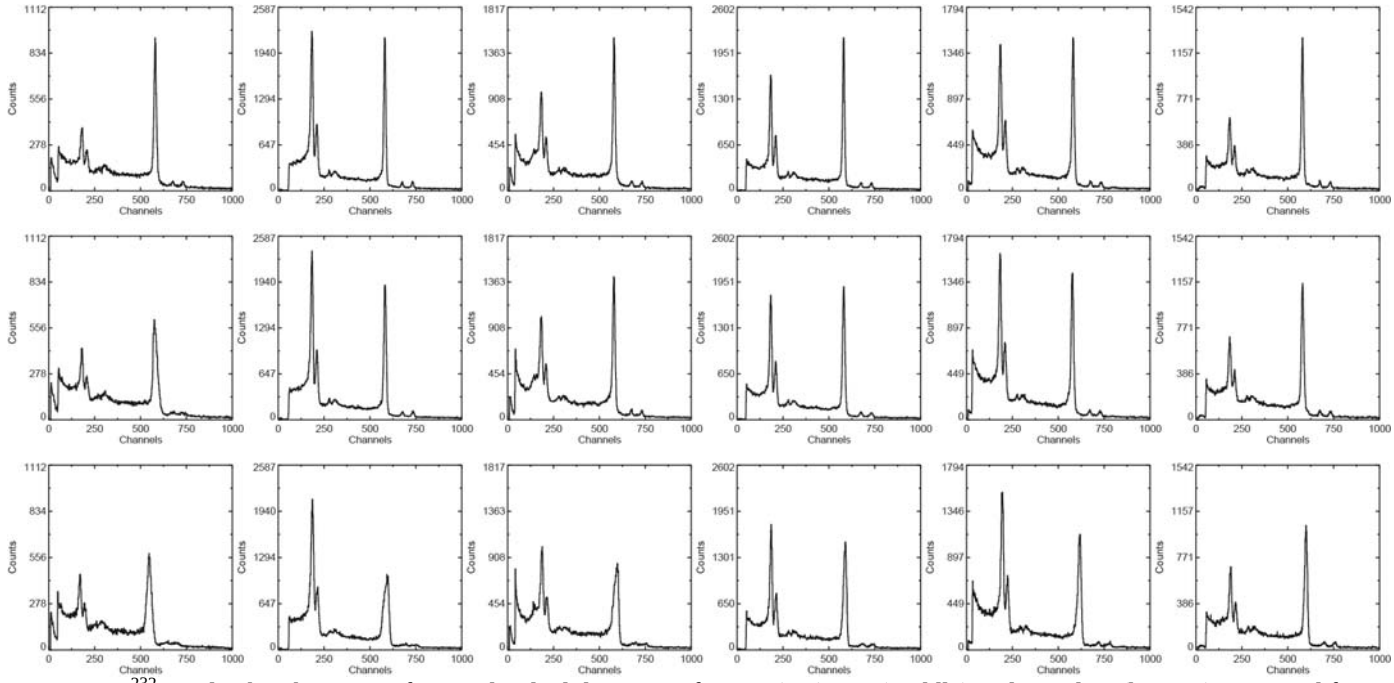

Figure 12. ^{232}U pulse-height spectra from individual detectors after 3D (top), 1D (middle) and raw data (bottom) measured for the detector configurations when all pads were interconnected. The temperature is 20 °C; the cathode bias is 2500 V. The energy resolution was in the range (2.0-2.2) % after the 3D corrections.

We would like to demonstrate the advantages of using the waveform readout approach, which was implemented here for a single detector only. A 6x6x20 mm^3 detector was mounted on the detector board, similar to the one used for the linear array, plugged into the motherboard inside a test box containing 6 charge-sensitive preamplifiers (eV-5093), whose inputs were connected to the anode, cathode and 4 pads. The waveforms were recorded using a LeCroy HDO 8058 oscilloscope. The signals, generated by a ^{137}Cs source, were sampled with 10-ns time intervals (bins) and stored in the oscilloscope's memory for further analysis. Fig. 13 shows an example of the digitized waveforms generated by the 662-keV photon in the detector.

For each acquired event, we used digitized waveforms from which we evaluated the signal amplitudes and timing information [12]. We used the cathode signal to find the event arrival time. The first ~100 sampling points of the cathode waveform are used to calculate the waveform's baseline and the standard deviation of the noise. The event arrival time is approximately located as the sample number at which the signal reaches greater than two standard deviations of noise above the baseline. Then, a narrow points segment around this sample is selected for the linear backward interpolation of the pulse's leading edge. The intersection of the interpolation line with the baseline gives the event arrival time. Next, we evaluated the electron cloud's arrival time to the anode. We define this time as an intersection of two lines: one extrapolated forward from the anode signal's leading edge and the second extrapolated backward from the pulse's saturated amplitude. Finally, the signal amplitudes are calculated as the difference between the saturated part of a waveform (a pulse height) and the baseline. The baseline is calculated by averaging the points within the time window adjacent from the left to the beginning of the pulse (event arrival time) [13-15]. The same size window located after the electron cloud arrival time and some delay is used to calculate the pulse level. The delay is necessary to shift the averaging window to minimize the effect of the rounded top of the pulse. The time window and the delay time are optimized to minimize the photopeak width.

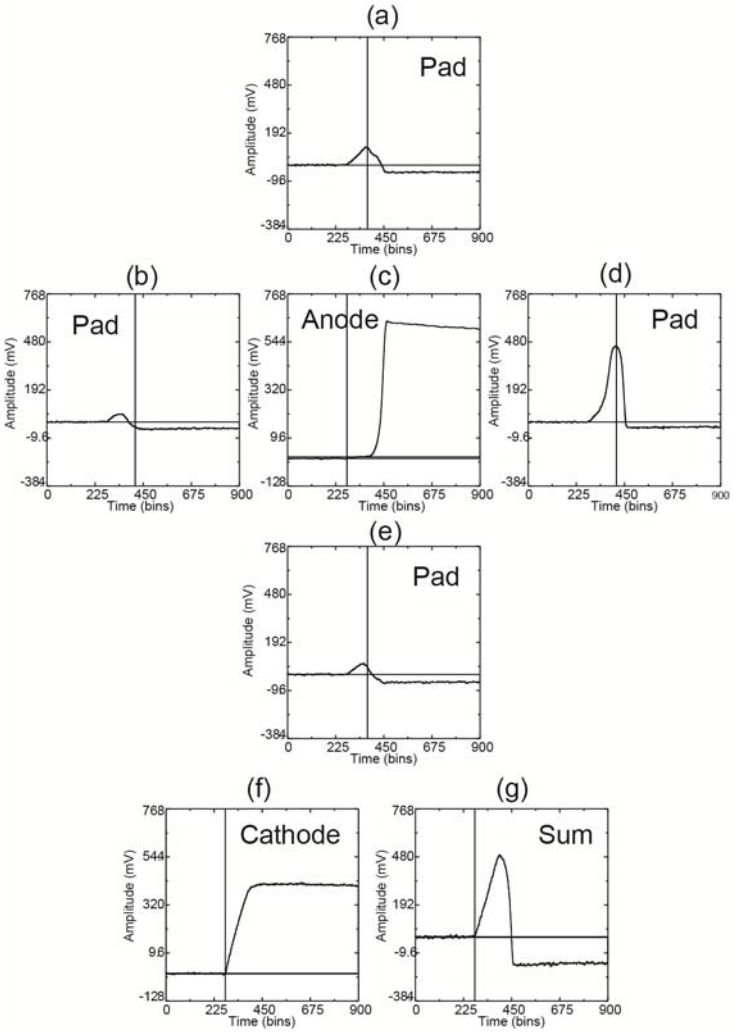

Figure 13. Waveforms captured from the cathode (f), the anode (c), and four pads (a, b, d, and e). Plot (g) represents the sum of the pad signals. The solid vertical line indicates the moment when the interaction occurs evaluated using the cathode signal.

In Fig. 13, the plots (a), (b), (d), and (e) represent the pad signals, while the plots (c) and (f) show the anode and the cathode signals. The solid vertical line indicates the moment when the interaction occur evaluated using the cathode signal. We note that, in our design the cathode is sensitive to the charges generated over the entire length of the crystal, so the cathode signals can be used for measuring the drift times and the interaction depths based on the cathode-to-anode ratio (*C/A*). The plot (g) represents the sum of the pad signals. The leading edge of the sum signal is almost identical to the leading edge of the cathode signal, which means that the sum of the pads signals can be used instead of the cathode signal. The most reliable and accurate way for identifying the location of the interaction point is to use the entire pad waveforms and the maximum-likelihood method to find the best fit to the benchmark waveforms obtained from calibration or simulated theoretically [14]. However, this approach requires very laborious calibrations. In this work, we used only one sample from each pad waveform (relative to the negative saturation portion of the signal) to evaluate the X-Y coordinates. We used the *C/A* (or *P/A* in the case of using the sum of the pads signals) ratio to evaluate the Z coordinate. Alternatively, the carriers' drift time could also be used to provide an independent estimate for the Z coordinate.

Figs. 14 (a) and (b) show correlations between the anode amplitudes and the interaction depth evaluated using the cathode (a) and the sum of the pad signals (b). As seen, the distributions are nearly identical which means the *P/A* ratio can be used to substitute for the *C/A* ratio. The same conclusion can be drawn from the correlations between the *C/A* (*P/A*) ratio and the drift time shown in Figs. 14 (c) and (d).

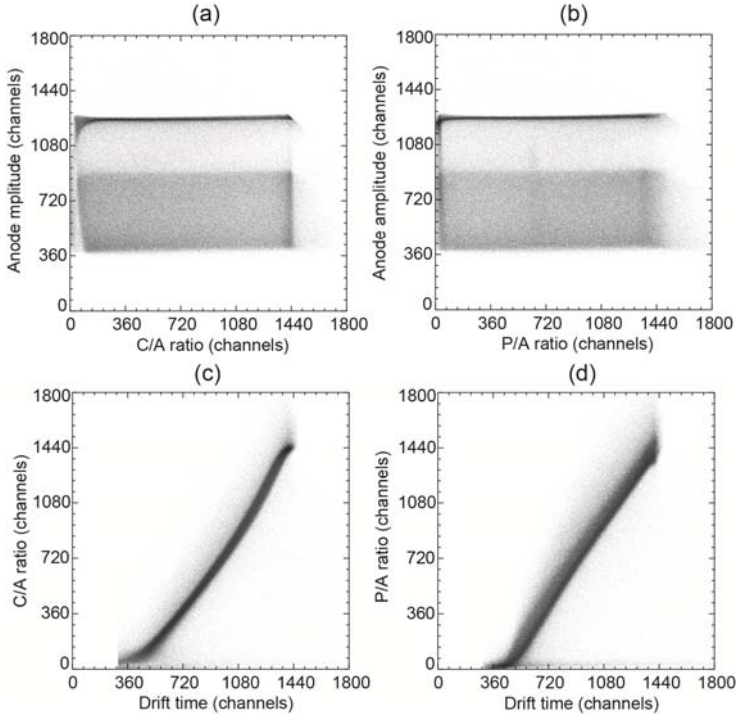

Figure 14. Comparison of correlations using C/A ratio and P/A ratio. (a) and (b) show the correlations between the anode amplitudes and the interaction depth. (c) and (d) show the correlation between the ratios and drift time.

Using digital waveform analysis allows us to improve position resolution, because we can use the time-correlated signals to evaluate X-Y coordinates. Originally we investigated this approach with pixelated detectors. However, here we applied it to VFG detectors. Fig. 15 (a,b) presents X-Y distributions of the charge-collection efficiency measured using a ^{137}Cs source for two different crystals (6x6 mm^2) using digital waveform analysis. The first image shows defects near the crystal edges resulting in complete signal losses, which are accurately revealed using positional information from the pads. The second crystal has a big defect located in the upper right side of the image. Fig. 15(c) demonstrates spatial resolution reconstruction using time-correlated signals created for a detector that had been damaged using a pulsed-laser system to 'write' the letters "BNL" on the surface of the crystal. The distortions within the letters are produced by crystal defects however the responses measured for each individual positions of the laser beam are very sharp considering the 9-µm fiber used for the laser irradiation. The ability to characterize crystal defects in such detail is an added benefit to the improvement of position resolution based on time-correlated samples.

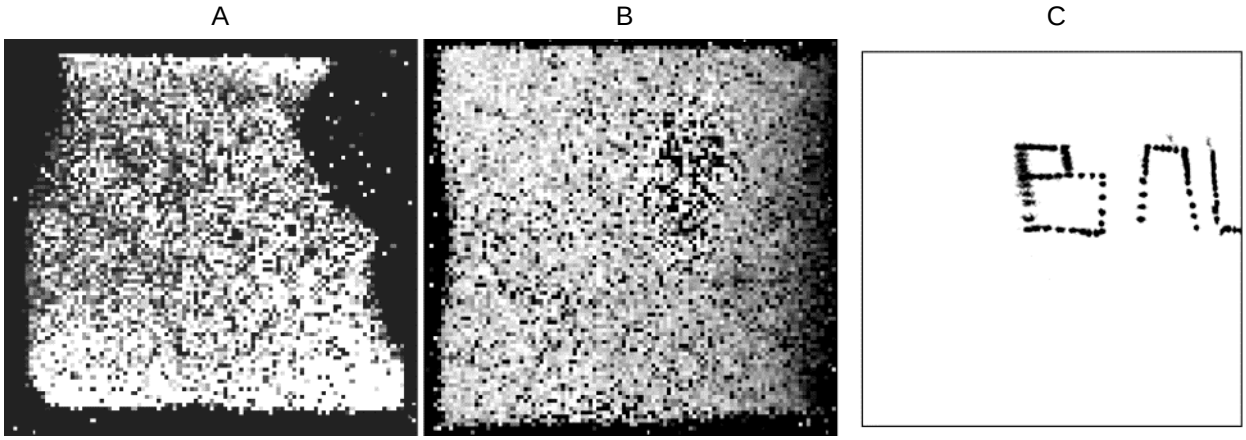

Figure 15. Crystal non-uniformities revealed in three different VFG detectors using the time-correlated signals to evaluate the X-Y coordinates. The third image shows the spatial reconstruction using a pulsed laser to write the letters "BNL". The total area of each detectors is 6x6 mm^2. The number of electrons created by the laser pulse corresponds to a deposited energy of ~ 1 MeV.

IV. Conclusions

We investigated the performance of a linear array of six position-sensitive VFG detectors optimized for usage in compact handheld instruments. One of our goals was to demonstrate the possibility of making a detector with a reduced number of readout channels. We demonstrated that we could combine several pads belonging to different detectors, because there is no leakage current on the charge-sensing pads. We were able to interconnect all pads in 4 groups and use only 4 individual inputs. We also demonstrated that 2 and even 4 cathodes could be connected to a single cathode input. Another goal was to evaluate the array under realistic field conditions. Detector responses were measured at different temperatures between 15 and 40 °C. The detectors could operate at a temperature close to 30 °C without significantly affecting the energy resolution. Above 30 °C the resolution degrades and approaches 2% at 662 keV at 40 °C. The results also showed that the correction matrix, used to perform the 3D corrections is independent of temperature over this range. Furthermore, the results illustrate the importance of temperature stability for the detectors within +/-1 degree °C. Lastly, it is optimal to use the correction matrix generated at a temperature that is close to or lower than the temperature at which measurements will be taken.

After applying corrections, the energy resolution was found to be 1.9 % FWHM at 186 keV. However, using only a 1D correction the energy resolution was only ~3 %. The original resolution before corrections was approximately 5.2 %. At a higher energy, the resolution can be as good as 0.8 % at 662 keV. These resolution improvements can significantly enhance the performance of compact handheld instruments.

To further study the capability of reducing the number of readout channels we investigated the possibility of interconnecting the corresponding pads from all the detectors, thus needing only 10 channels to read signals from 4 pads and 6 anodes. This also simplifies the detector design by eliminating decoupling capacitors and the cathode signals wires.

Furthermore, one can avoid using an ASIC by replacing it with hybrid preamplifiers and a 10-channel digitizer. We demonstrated that the waveform analysis allows us to use the *Pad/Anode* ratio to substitute for the *Cathode/Anode* ratio. The same conclusion can be drawn from the correlations between the *C/A* (*P/A*) ratio and the drift time. This allows developers to simplify the detector design and improve the instrument performance.

References

[1] A. E. Bolotnikov, G. S. Camarda, Y. Cui, G. De Geronimo, J. Fried, A. Hossain, K. Lee, G. Mahler, M. Maritato, M. Marshall, M. Petryk, U. Roy, E. Vernon, G. Yang and R. B. James, “Use of high-granularity position sensing to correct response non-uniformities of CdZnTe detectors”, Appl. Phys. Lett. 104, p. 263503, 2014.

[2] A. E. Bolotnikov, G. S. Camarda, E. Chen, S. Cheng, Y. Cui, R Gul, R. Gallagher, V. Dedic, G. De Geronimo, L. Ocampo Giraldo, J. Fried, A. Hossain, J. M. MacKenzie, P. Sellin, S. Taherion, E. Vernon, G. Yang, U. El-hanany and R. B. James, “CdZnTe Position-Sensitive Drift Detectors with Thicknesses Up to 5 cm”, Appl. Phys. Lett. 108, p. 093504 (2016).

[3] L. Ocampo Giraldo, A.E. Bolotnikov, G.S. Camarda, S. Cheng, G. De Geronimo, A. McGilloway, J. Fried, D. Hodges, A. Hossain, K. Ünlü, M. Petryk, V. Vidal, E. Vernon, G. Yang, R. B. James, "Arrays of Position-Sensitive Virtual Frisch-Grid CdZnTe Detectors: Results From a 4x4 Array Prototype," in IEEE Transactions on Nuclear Science, vol. 64, no. 10, pp. 2698-2705, Oct. 2017.

[4] V. V. Dmitrenko, A. C. Romanuk, Z. M. Uteshev, and V. K. Chernyatin, “Spectrometric applications of an ionization-type drift chamber”, Pribory I Tekhnika Eksperimenta, vol. 1, pp. 51-53, 1982. Translation in Instruments and Experimental Techniques (USA), vol. 25, no. 1, pp. 50-53 (1982).

[5] K. Parnham, C. Szeles, K. G. Lynn, and R. Tjossem, "Performance Improvement of CdZnTe Detectors Using Modified Two-Terminal Electrode Geometry," in Hard X-ray, Gamma-Ray and Neutron Detector Physics, Proceedings of SPIE Vol. 3786, pp. 49-54, 1999.

[6] C. Szeles, D. Bale, J. Grosholz, Jr., G. L. Smith, M. Blostein, and J. Eger, “Fabrication of High Performance CdZnTe Quasi-Hemispherical Gamma-ray CAPture™ Plus Detectors”, Hard X-Ray and Gamma-Ray Detector Physics VIII, edited by Larry A. Franks, Arnold Burger, and Ralph B. James, Proceedings of SPIE Vol. 6319 (SPIE, Bellingham, WA, 2006).

[7] D. S. McGregor and R. A. Rojeski, “High-resolution ionization detector and array of such detectors”, US Pat. 6175120, 2001.

[8] G. Montemont, M. Arques, L. Verger, and J. Rustique, “A Capacitive Frisch Grid Structure for CdZnTe Detectors”, IEEE Trans. Nucl. Sci. 48, pp. 278-281, 2001.

[9] A. E. Bolotnikov, K. Ackley, G. S. Camarda, C. Cherches, Y. Cui, G. De Geronimo, J. Fried, D. Hodges, A. Hossain, W. Lee, G. Mahler, M. Maritato, M. Petryk, U. Roy, C. Salwen, E. Vernon, G. Yang, and R. B. James, “An array of virtual Frisch-grid CdZnTe detectors and a front-end application-specific integrated circuit for large-area position-sensitive gamma-ray cameras,” Review of Scientific Instruments, vol. 86, no. 7, 2015.

[10] G. De Geronimo, E. Vernon, K. Ackley, A. Dragone, J. Fried, P. O’Connor, Z. He, C. Herman, and F. Zhang, “Readout ASIC for 3-D position-sensitive detectors,” IEEE Trans. Nucl. Sci., vol. 55, no. 3, pp. 1593–1603, 2008.

[11] E. Vernon, K. Ackley, G. De Geronimo, J. Fried, P. O’Connor, Z. He, C. Herman, and F. Zhang, “ASIC for high rate 3-D position sensitive detectors,” IEEE Trans. Nucl. Sci., vol. 57, no. 3, pp. 1536–1542, 2010.

[12] F. Zhang, C. Herman, Z. He, G. De Geronimo, E. Vernon, and J. Fried, “Characterization of the H3D ASIC readout system and 6.0 cm^3 3-D position sensitive CdZnTe Detectors,” IEEE Trans. Nucl. Sci. 59, pp. 236-242, 2012.

[13] A. E. Bolotnikov, J. Butcher, G. S. Camarda, Y. Cui, G. De Geronimo, J. Fried, R. Gul, P. M. Fochuk, M. Hamade, K. H. Kim, O. V. Kopach, M. Petryk, E. Vernon, G. Yang, and R. B. James, "Array of Virtual Frisch-Grid CZT Detectors With Common Cathode Readout for Correcting Charge Signals and Rejection of Incomplete Charge-Collection Events," IEEE Transactions on Nuclear Science, vol. 59, no. 4, pp. 1544-1551, 2012.

[14] L. Ocampo Giraldo, A. E. Bolotnikov, G. S. Camarda, S. Cheng, G. De Geronimo, A. McGilloway, J. Fried, D. Hodges, A. Hossain, K. Ünlü, M. Petryk, V. Vidal, E. Vernon, G. Yang, R. B. James, “Using a pulsed laser beam to investigate the feasibility of sub-pixel position resolution with time-correlated transient signals in 3D pixelated CdZnTe detectors”, Nucl. Instrum. And Methods, A867, pp.7-14, 2017.

[15] A. E. Bolotnikov, G. S. Camarda, Y. Cui, A. Hossain, G. Yang, H. W. Yao, and R. B. James, “Internal electric-field-lines distribution in CdZnTe detectors measured using X-ray mapping”, IEEE Trans. Nucl. Sci. 56, pp. 791-794, 2009.